

Electrical Detection of Magnetic Skyrmions in a Magnetic Tunnel Junction

Yao Guang, Like Zhang, Junwei Zhang, Yadong Wang, Yuelei Zhao, Riccardo Tomasello, Senfu Zhang, Bin He, Jiahui Li, Yizhou Liu, Jiafeng Feng, Hongxiang Wei, Mario Carpentieri, Zhipeng Hou, Junming Liu, Yong Peng, Zhongming Zeng, Giovanni Finocchio,* Xixiang Zhang, John Michael David Coey, Xiufeng Han, and Guoqiang Yu*

Magnetic skyrmions are promising information carriers for dense and energy-efficient information storage owing to their small size, low driving-current density, and topological stability. Electrical detection of skyrmions is a crucial requirement to drive skyrmion devices toward applications. The use of a magnetic tunnel junction (MTJ) is commonly suggested for this purpose as MTJs are key spintronic devices for large-scale commercialization that can convert magnetic textures into electrical signals. To date, however, it has been challenging to realize skyrmions in MTJs due to incompatibility between standard skyrmion materials and highly efficient MTJ electrodes. Here, a material stack combining magnetic multilayers, which host 100 nm scale skyrmions, with a perpendicularly magnetized MTJ, is reported. The devices are designed so that the skyrmions in the multilayer are imprinted into the MTJ's free layer via magnetostatic interactions. The electrical response of a single skyrmion is successfully identified by employing simultaneous imaging of the magnetic texture and the electrical measurement of the MTJ resistance. The results are an important step toward all-electrical detection of skyrmions.

1. Introduction


Microelectronic technology can be envisaged that will take advantage from the unique combination of small size, high mobility, and topological stability that magnetic skyrmions offer.^[1,2] They are promising as high-density information carriers, either in conventional low-energy consumption memory applications^[3–5] and voltage-controlled non-volatile memory,^[6] or in unconventional applications, including probabilistic and neuromorphic computing.^[7–9] Following the first experimental observation of skyrmions,^[10,11] a fruitful research program has revealed many single crystals with particular symmetries hosting Bloch-type skyrmions^[10–14] and antiskyrmions,^[15–17] as well as Néel-type skyrmions stabilized

Y. Guang, B. He, J. Li, Y. Liu, J. Feng, H. Wei, X. Han, G. Yu
Beijing National Laboratory for Condensed Matter Physics
Institute of Physics
Chinese Academy of Sciences
Beijing 100190, China
E-mail: guoqiangyu@iphy.ac.cn

Y. Guang, B. He, J. Li, J. Feng, X. Han, G. Yu
Center of Materials Science and Optoelectronics Engineering
University of Chinese Academy of Sciences
Beijing 100049, China

Y. Guang, X. Han, G. Yu
Songshan Lake Materials Laboratory
Dongguan, Guangdong 523808, China

L. Zhang, Z. Zeng
Nanofabrication Facility
Suzhou Institute of Nano-Tech and Nano-Bionics
Chinese Academy of Sciences
Suzhou, Jiangsu 215123, China

 The ORCID identification number(s) for the author(s) of this article can be found under <https://doi.org/10.1002/aelm.202200570>.

© 2022 The Authors. Advanced Electronic Materials published by Wiley-VCH GmbH. This is an open access article under the terms of the Creative Commons Attribution License, which permits use, distribution and reproduction in any medium, provided the original work is properly cited.

DOI: 10.1002/aelm.202200570

J. Zhang, Y. Peng
School of Materials and Energy
Electron Microscopy Centre of Lanzhou University and Key Laboratory of Magnetism and Magnetic Materials of the Ministry of Education
Lanzhou University
Lanzhou 730000, China

Y. Wang, Z. Hou, J. Liu
Guangdong Provincial Key Laboratory of Optical Information Materials and Technology & Institute for Advanced Materials
South China Academy of Advanced Optoelectronics
South China Normal University
Guangzhou 510006, China

Y. Zhao, S. Zhang, X. Zhang
Physical Science and Engineering Division (PSE)
King Abdullah University of Science and Technology (KAUST)
Thuwal 23955–6900, Saudi Arabia

R. Tomasello, M. Carpentieri
Department of Electrical and Information Engineering
Politecnico di Bari, Bari 70125, Italy

S. Zhang
Key Laboratory of Magnetism and Magnetic Materials of the Ministry of Education
Lanzhou University
Lanzhou 730000, China

in thin-film heterostructures.^[18–28] However, an outstanding challenge has been the development of an efficient electrical detection mechanism which will be the key to the development of magnetic skyrmion-based technology. A variety of attempts have proved that it is possible to detect skyrmions electrically through topological Hall effect,^[1,29,30] tunneling non-collinear magnetoresistance,^[31] anisotropic magnetoresistance,^[32] anomalous Hall effect,^[33,34] and anomalous Nernst effect.^[35,36] The resistivity and voltage changes corresponding to a single skyrmion are about 20–30 nΩ cm when using the anomalous Hall effect and 90 nV when using the anomalous Nernst effect (temperature gradient 0.9 K μm⁻¹). A potentially efficient alternative read-out mechanism is based on the tunneling magnetoresistance (TMR) realized in a magnetic tunnel junction (MTJ) as proposed theoretically,^[37–39] and explored in some recent experiments.^[40–42] However, it is challenging to tailor the state-of-the-art skyrmion materials that host small room-temperature skyrmions in MTJ with an MgO barrier,^[42] which is the key to realizing high TMR ratio. Here, we propose and demonstrate a strategy to combining materials developed to stabilize and manipulate small skyrmions with a perpendicularly magnetized MTJ stack having a TMR of about 20% at room temperature. This strategy, also applicable to other materials that host skyrmions, opens a promising route to realizing skyrmion detection using MTJs. In addition, we have measured the MTJ resistance change corresponding to a single skyrmion, having a diameter of 100 nm, combining electrical transport measurements with direct imaging of magnetic texture by magnetic force microscopy (MFM), as shown in Figure 1.

The materials stack is designed to imprint the magnetic domain pattern of the multilayer into the MTJ's free layer via magnetostatic interactions. The evolution of the magnetic domain pattern is revealed by MFM, which shows that skyrmions can be stabilized in the fabricated MTJ with an appropriate magnetic field. The realization of electrical reading of skyrmions using an MTJ opens the route to all-electrical skyrmion devices, which is a crucial step for the development of skyrmionics. The technique reported here can further advance the simultaneous optimization of the parameters for skyrmion stabilization and MTJ read-out, thus opening a way to realize skyrmion-based devices such as racetrack memory,^[3–5] logic gates,^[43,44] oscillators,^[45,46] detectors,^[47] artificial synapses for neuromorphic computing,^[48,49]

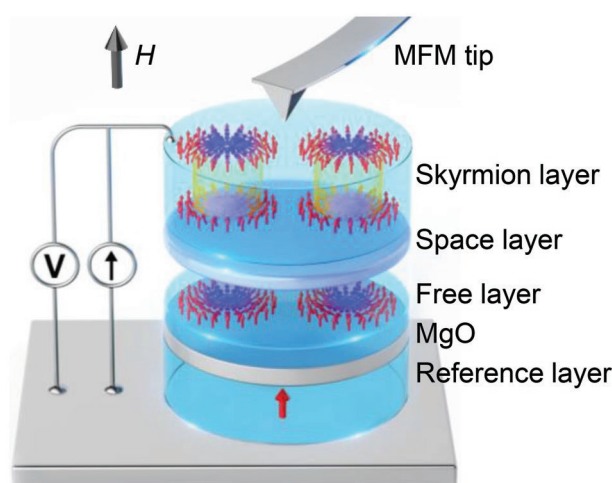


Figure 1. A schematic of the detection of skyrmions in a magnetic tunnel junction (MTJ). The bottom reference layer, MgO layer, and free layer constitute the MTJ. The skyrmion layer hosts room-temperature skyrmions, which can be imprinted into the free layer through magnetostatic interaction. Electrical measurement and magnetic force microscopy (MFM) imaging were simultaneously performed to determine the magnetoresistive signal of the MTJ corresponding to a single skyrmion.

and reshuffling devices^[8] with an efficient CMOS compatible read-out mechanism.^[39,50]

2. Structural and Magnetic Characterization of Magnetic Tunnel Junction Films

The device stack is shown in Figure 2a. It consists of Si/SiO₂/Ta (2)/Ru (5)/Pt (2)/[Co (0.28)/Pt (0.16)]₉/Co (0.28)/Ru (0.4)/Co (0.28)/[Pt (0.16)/Co (0.28)]₅/Ta (0.2)/Co₄₀Fe₄₀B₂₀ (0.8, reference layer)/MgO (2.5)/Co₂₀Fe₆₀B₂₀ (*t*_{CoFeB} = 1.2, 1.3, 1.4, or 1.5, free layer)/Ta (2)/[Pt (3)/Co (2)/Ta (2)]₁₀/Pt (2) (thickness in nm). The MgO layer, together with the two adjacent CoFeB layers, constitute the MTJ. The bottom CoFeB reference layer is perpendicularly magnetized and pinned by the synthetic antiferromagnet (SAF) layers. The top CoFeB free layer is magnetically coupled to the skyrmion multilayers ([Pt/Co/Ta]₁₀), where skyrmions are stabilized by competition among the interfacial Dzyaloshinskii–Moriya interaction (DMI), perpendicular magnetic anisotropy, external, and dipolar fields.^[51–53] Figure 2b shows the transmission electron microscopy (TEM) image of the film with *t*_{CoFeB} = 1.5 nm, which exhibits a high-quality layered structure and interfaces. Similar quality is also achieved for different *t*_{CoFeB}. Figure 2c shows the out-of-plane magnetic hysteresis loop for the MTJ film with the representative configurations of the magnetic layers at different field values. Upon increasing the magnetic field from a negative maximum (red curve), the two parallel magnetic moments (blue and grey arrows) progressively evolve into an antiferromagnetic state at around –630 mT due to the antiferromagnetic coupling of the SAF layers. With further increase of the magnetic field, an abrupt switch is observed at about –130 mT, and then as the magnetic field increases the magnetic state of the skyrmion layer (red arrow) switches to the positive direction via the nucleation and the spatial evolution of a multidomain state. At the field

J. Liu
Laboratory of Solid State Microstructures and Innovation
Center of Advanced Microstructures
Nanjing University
Nanjing 211102, China

G. Finocchio
Department of Mathematical and Computer Sciences
Physical Sciences and Earth Sciences
University of Messina
Messina 98166, Italy
E-mail: giovanni.finocchio@unime.it

J. M. D. Coey
CRANN
AMBER and School of Physics
Trinity College Dublin
Dublin 2, Ireland

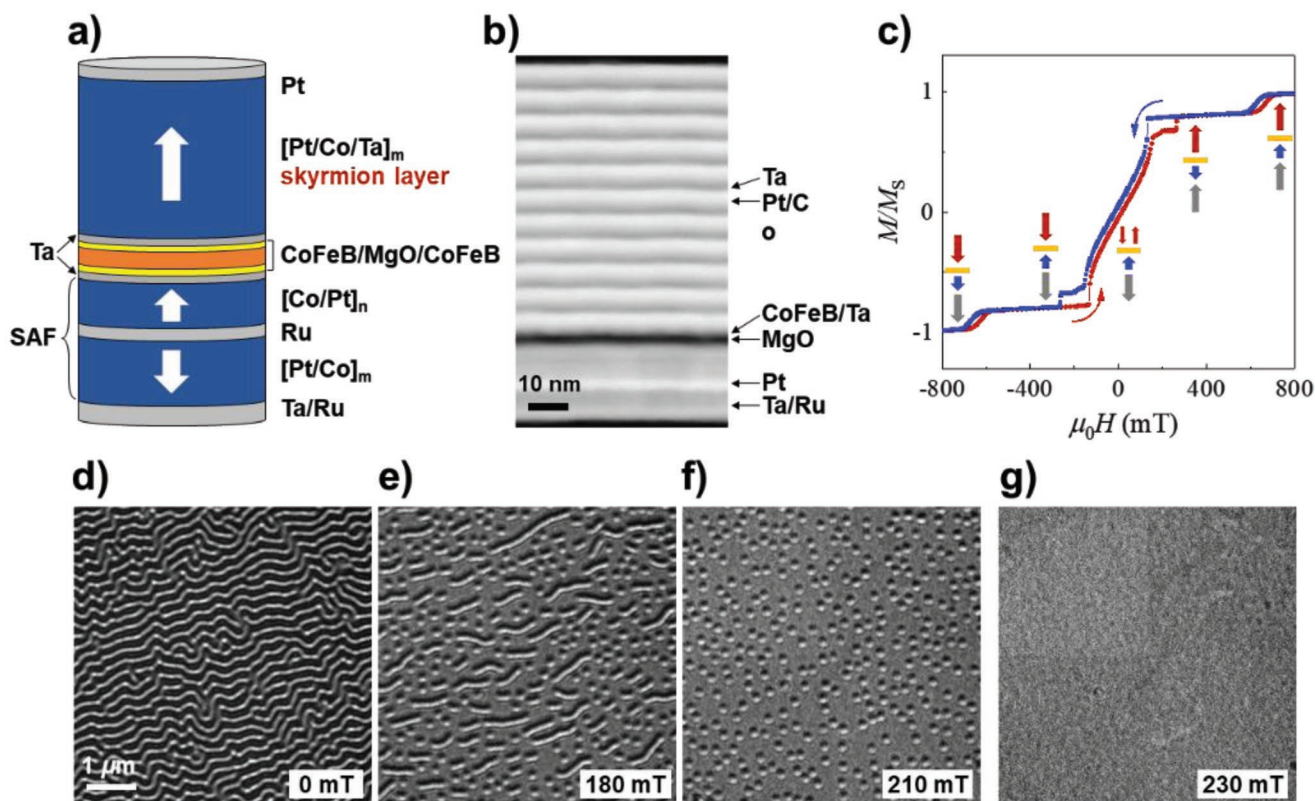


Figure 2. Sample structure and skyrmions in the MTJ films. a) A sketch of the MTJ. The skyrmion layer consists of $[\text{Pt} (3)/\text{Co} (2)/\text{Ta} (2)]_{10}/\text{Pt} (2)$ (thickness in nm). The free layer of the MTJ, that is, the top yellow CoFeB layer ($t_{\text{CoFeB}} = 1.2, 1.3, 1.4,$ or 1.5), is magnetically coupled to the skyrmion layer. The reference layer, that is, the bottom yellow CoFeB layer, is pinned by the SAF. The SAF consists of $\text{Pt} (2)/[\text{Co} (0.28)/\text{Pt} (0.16)]_5/\text{Co} (0.28)/\text{Ru} (0.4)/\text{Co} (0.28)/[\text{Pt} (0.16)/\text{Co} (0.28)]_5$. The white arrows refer to the magnetic moment of the corresponding magnetic layers in the SAF. b) High-resolution TEM image of the cross-section of the MTJ films. c) Magnetic hysteresis loop of the MTJ film with $t_{\text{CoFeB}} = 1.2$ nm. The inset arrows show the magnetic configurations of the different layers for the magnetic field swept from the negative direction to the positive direction. The red, blue, and gray arrows refer to the skyrmion layer and CoFeB free layer, the CoFeB reference layer and top magnetic part of the SAF, and the bottom magnetic part of the SAF. d–g) The evolution of the magnetic domain pattern for the sample with $t_{\text{CoFeB}} = 1.2$ nm, which is captured by Lorentz electron transmission microscopy (LTEM).

of 260 mT, another abrupt switch is observed, corresponding to the flip of the net magnetic moment of the SAF layers. Further increasing the magnetic field along the positive direction leads to the positive parallel alignment of the SAF moments again. It is noted that the hysteresis loops for different CoFeB layer thicknesses (1.2–1.5 nm) are very similar (as shown in Figure S1, Supporting Information), which indicates that the CoFeB layer is coupled to the skyrmion layer through magnetostatic interactions in all these samples, as also confirmed by micromagnetic simulations and electrical measurements shown later in the text.

To capture the detailed spin textures of the skyrmion layer in the MTJ films we used Lorentz transmission electron microscopy (LTEM). We mainly used the Fresnel method to observe the skyrmion. LTEM measurements were carried out at -30.5° . When the magnetic field is zero, a typical maze domain pattern is formed with a periodicity of about 190 nm (see Figure 2d). Upon increasing the magnetic field, the stripe domains are gradually transformed into skyrmions, as shown in Figure 2e, and eventually the skyrmion phase is stabilized (see Figure 2f). We highlight that the observed bright and dark contrasts correspond to skyrmions, as it has been well demonstrated in previous work.^[54–56] The LTEM measurements of

the skyrmions have also been performed at different tilt angles $30.5^\circ, 0^\circ,$ and -30.5° . As shown in Figure S2, Supporting Information, the contrast disappears at 0° and reverses for opposite tilt angles of the sample, which are the characteristic features measured of a Néel skyrmion.^[57] The film magnetization exhibits a single domain state when the field is 230 mT, as shown in Figure 2g.

3. Electrical and Magnetic Characterization of Magnetic Tunnel Junction Devices

The films were patterned into MTJ devices with a circular cross section, as shown in Figure 3a, having different diameters (5, 4, 3, and 2 μm). For $t_{\text{CoFeB}} = 1.2$ nm, the MTJs exhibit a TMR ratio of about 20% and a similar resistance-area-product (RA), as shown in Figures S3 and S4, Supporting Information. These cross sections have been chosen to enable simultaneous electrical measurements and magnetic imaging. The TMR ratio is defined by $\text{TMR} = (R_{\text{AP}} - R_{\text{P}})/R_{\text{P}}$. The R_{AP} (R_{P}) is the resistance of the antiparallel (parallel) state. A typical TMR loop for a 3 μm diameter MTJ is shown in Figure 3b. As expected, the switching fields in the RH loop are similar to those in the MH

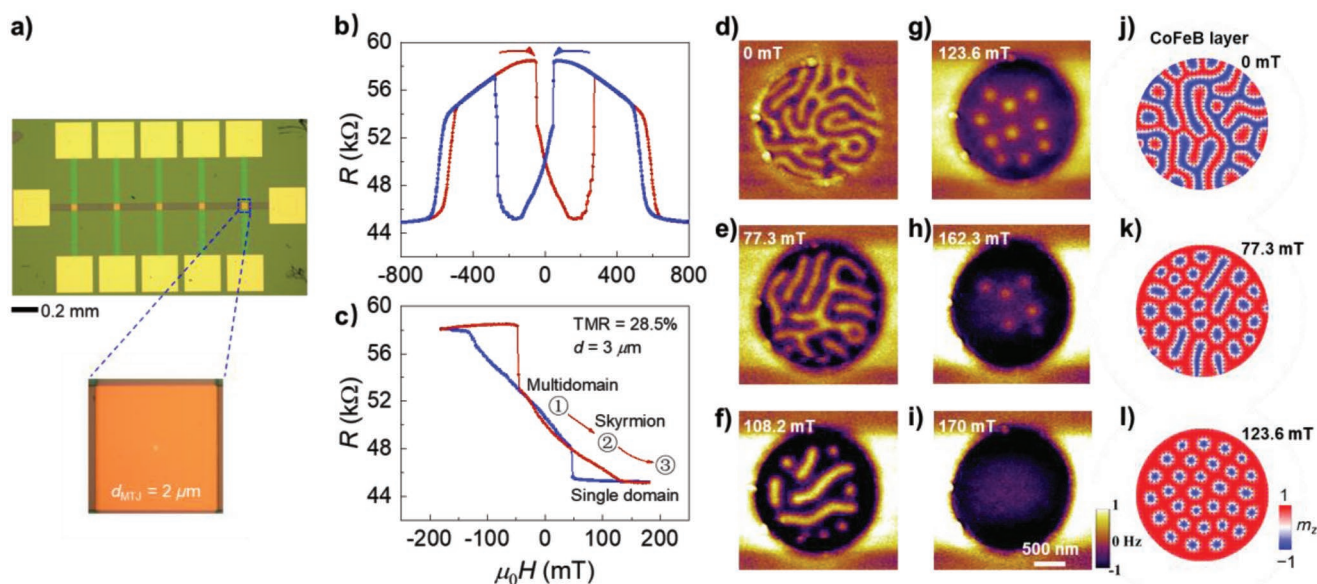


Figure 3. MFM imaging of skyrmions in the MTJ. a) Optical microscopy image of the MTJ device and junction area. b) Out-of-plane magnetoresistance hysteresis loop for a MTJ with $t_{\text{CoFeB}} = 1.2$ nm. The MTJ has a TMR ratio of 28.5% and a junction diameter of $3 \mu\text{m}$. c) The minor resistance hysteresis loop. At zero field (labeled by ①), the skyrmion layer has a maze domain structure. With the increase of magnetic field in the positive direction, the domain is changed to a skyrmion phase (labeled by ②) and eventually to a single domain (labeled by ③). The skyrmion layer remains in a single domain if the magnetic field is slightly reduced. d–i) MFM images of domain structures in the MTJ with the $t_{\text{CoFeB}} = 1.5$ nm and the diameter of $2 \mu\text{m}$ at different magnetic fields. j–l) Micromagnetic simulations describing the magnetic evolution of the magnetic texture (red/blue indicate positive/negative z-component of the magnetization) in the CoFeB free layer of the MTJ, the diameter used for calculation is $1.2 \mu\text{m}$.

loop of the MTJ films, again indicating that the CoFeB layer is nicely coupled to the skyrmion layer because the RH loop is only sensitive to the magnetization of the CoFeB layer. The magnetic coupling can also be directly reflected by the difference between the RH loops of the studied sample and the control sample without a skyrmions layer (see Figure S5, Supporting Information). Considering the minor RH loop shown in Figure 3c, the CoFeB free layer is flipped within this field range because it is magnetically coupled to the skyrmion layer. The low (high) resistance corresponds to the parallel (antiparallel) state. Under the magnetic field of -200 mT, the MTJ is in a high resistance state, corresponding to the antiparallel state of the free and reference layers. The high resistance state remains with the increase of the magnetic field up to -50 mT. When the magnetic field is further increased, the MTJ resistance jumps down suddenly, corresponding to the transition from a single domain state to a multidomain state. Once the magnetic field is close to zero, a typical maze domain pattern is formed (Figure 3d), similar to what has been found in the continuous film (Figure 2d). In this state, the up and down domains have nearly equal areas, resulting in a resistance in a range between R_{AP} and R_{P} . With the increase of magnetic field along the positive direction, the MTJ resistance continuously decreases, corresponding to a reduction of the down domain area (see Figure 3e). This evolution of the magnetic domains is revealed by MFM imaging. Consistent with the unpatterned films as imaged by the LTEM, as the field increases some stripe domains gradually transformed into skyrmions (Figure 3f), and finally a skyrmion phase is stabilized, as shown in Figure 3g. A further increase of the field leads to a reduction of the skyrmion density and a shrinkage of their diameter (see Figure 3h).

For magnetic fields larger than 170 mT, all the skyrmions are annihilated and a single domain is stabilized (see Figure 3i). The experimental results on the field evolution of the magnetic texture are quantitatively confirmed by micromagnetic simulations (see Experimental Section for numerical details). Figure 3j–l show snapshots of the CoFeB free layer for a direct comparison (red/blue is positive/negative magnetization) with the experimental observations at 0 , 77.3 , and 123.6 mT. The configuration is stabilized in this layer via the magnetostatic interactions, and the imprinted chirality is the same as that in the adjacent layer of the skyrmion-generating stack. The skyrmions exhibit a hybrid profile along the sample thickness direction (see Note S1 and Figure S8b,c, Supporting Information) where the bottom and top ferromagnetic layers host a Néel skyrmion with radially outward and inward-pointing spins, respectively, due to magnetostatic interactions.^[51,52,58] In addition, micromagnetic simulations show that this profile is slightly dependent on the presence/absence of the free layer (not shown).

4. Electric Detection of Skyrmions in an MTJ

We next focus on extracting the electrical signal for a single skyrmion by combining MFM imaging and electrical measurement on an MTJ with a diameter of $3 \mu\text{m}$. Similar results have been achieved for MTJs with other diameters. Figure 4a–g shows a series of magnetic domain states as a function of the out-of-plane field. We note that the MFM image of the MTJ junction area is slightly distorted due to the influence of the magnetic field on the probe holder. The distortion has been

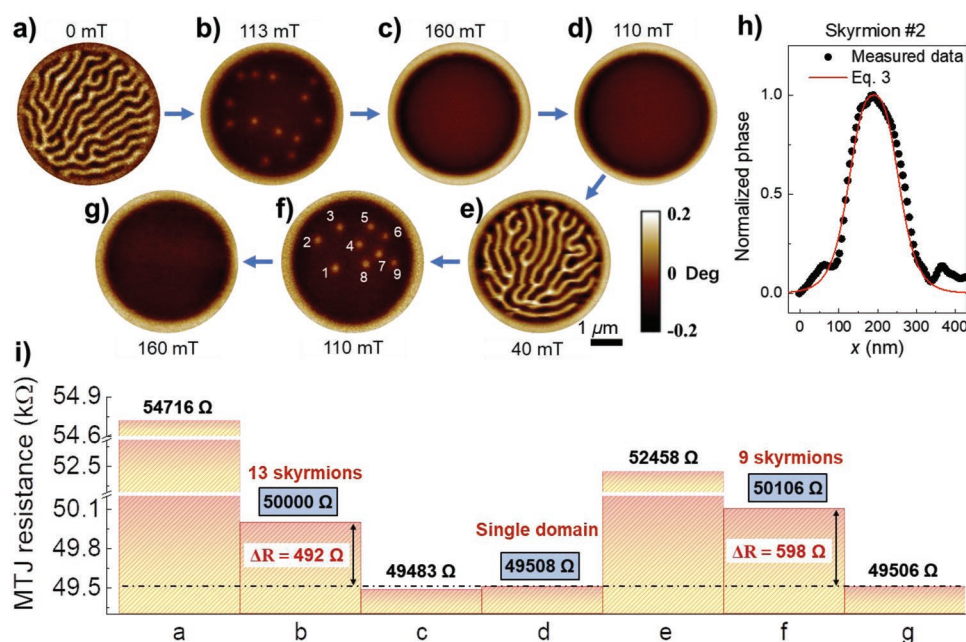


Figure 4. Electrical detection of magnetic skyrmions in the MTJ. a–g) MFM images of domain structures in the MTJ junction with $t_{\text{CoFeB}} = 1.5$ nm and junction size of 3 μm at different magnetic fields. h) MFM phase data for the skyrmion #2 in (f) and the analytical skyrmion profile obtained from Equation (3). i) The resistances of the MTJ corresponding to MFM images in (a–g). The resistance plotted is obtained by averaging the resistance measured before and after the MFM imaging. The dashed line indicates the resistance for the single domain state at a magnetic field of 110 mT (state d).

corrected based on the circular shape of the MTJ device. The original images are shown in Figure S6, Supporting Information. The profile of skyrmion #2 is shown in Figure 4h, which fits well with the theoretical model (see Experimental Section). The average radius of the skyrmion extracted from MFM data is $r_{\text{sky}} = 70$ nm. The corresponding resistance is obtained by averaging the measured MTJ resistance before and after the MFM imaging experiment. The applied current for reading the resistance is 0.1 μA . The resistances before and after the imaging procedure are almost identical, and the averaged resistances for each state are shown in Figure 4i. To obtain the electrical signal originating from a single skyrmion, we compare the resistances between the skyrmion phase and single-domain states, such as b and d as well as f and d. The MTJ resistance in the skyrmion phase has a higher value as compared to that of a single domain state because the core area of the skyrmion has the magnetization antiparallel to that of the reference layer. The total resistance increase compared to state d is 492 Ω , which is due to the existence of 13 skyrmions that causes the increase of the area of antiparallel magnetization. Therefore, the resistance change for each skyrmion is about 38 Ω , assuming the skyrmions are all in the same size. For the f state with 9 skyrmions, the resistance increase is 598 Ω . Therefore, the resistance change for each skyrmion is about 66 Ω (again, assuming the skyrmions are the same in size). The difference in the skyrmion resistance between the states b and f is likely because there is some difference in diameter and profile for different skyrmions (see Figure S7, Supporting Information), which may originate from the different field sweeping history.

Considering a simple model, for a given skyrmion diameter the change of resistance per unit area can be estimated using the following equation: $\Delta R = \text{TMR} \frac{A_{\text{sky}}}{A_{\text{MTJ}}} R_p$, where A_{sky} and A_{MTJ}

are the areas for a single skyrmion and the MTJ, respectively. Considering the radius of $r_{\text{sky}} = 70$ nm, $r_{\text{MTJ}} = 1.5$ μm , and the TMR ratio of 26.7% for the minor loop of the MTJ are shown in Figure 4, the ΔR is determined to be 29 Ω , which is reasonably close to the experimental results (38 or 66 Ω). We can also estimate the change of resistance per single skyrmion from the micromagnetic simulations for a skyrmion in the CoFeB free layer and top Co layer of Figure 3l, respectively, as a function of the external field, of the number of repetitions of the $[\text{Pt}/\text{Co}/\text{Ta}]_n$, as well as of the MTJ diameter (see Note S1, Supporting Information).

It is important to compare the electrical response of a single skyrmion obtained via MTJ and those obtained with other techniques. In this work, using the MTJ with a TMR ratio of 26.7%, the resistance change corresponding to a single skyrmion is in the range from 38 to 66 Ω . This is significantly larger than the resistance change achieved with the AHE for skyrmion reading (in the range of m Ω).^[33,34] For skyrmion readout using the anomalous Nernst effect,^[35,36] where a 3 mA current is used to generate the thermal gradient, the voltage change for a single skyrmion is 90 nV. In our case, the reading current is 0.1 μA , the voltage change corresponding to the resistance change is in the range of 3.8 to 6.6 μV , which is also larger than using the anomalous Nernst effect. Except for the enhancement of the read-out signal, the two-terminal reading configuration is more convenient for device applications, and there is still room for improvement considering that the state-of-the-art MTJs have a TMR ratio that can reach more than 200%.^[59] The perpendicular magnetic anisotropy of the reference layer, the annealing processing, and the thickness of the layer can be further optimized to increase the TMR ratio.

5. Summary and Conclusions

We have demonstrated the electrical read-out of magnetic skyrmions using an MTJ device combining a multilayer hosting skyrmions and an MTJ in the same stack. The skyrmion phase stabilized in the skyrmion multilayer is imprinted onto the free layer of MTJ and then read out via the TMR. The electrical signal corresponding to a single skyrmion is in the range from 38 to 66 Ω , which is significantly enhanced compared to the anomalous Hall effect and anomalous Nernst effect. This work not only demonstrates the feasibility of reading skyrmions using an MTJ, but it also enables the development applications where it can be reduced area occupancy and/or power consumption by using skyrmion-based devices as compared to the microelectronic technology.

6. Experimental Section

Experimental Details: The samples consisting of Si/SiO₂/Ta (2)/Ru (5)/Pt (2)/[Co (0.28)/Pt (0.16)]₉/Co (0.28)/Ru (0.4)/Co (0.28)/[Pt (0.16)/Co (0.28)]₅/Ta (0.2)/Co₄₀Fe₄₀B₂₀ (0.8)/MgO (2.5)/Co₂₀Fe₆₀B₂₀ (*t*_{CoFeB} = 1.2, 1.3, 1.4, or 1.5)/Ta (2)/[Pt (3)/Co (2)/Ta (2)]₁₀/Pt (2) (thickness in nm) were deposited on a semi-insulating Si substrate with 100 nm thick thermally formed SiO₂ layer by a magnetic sputtering system. For the LTEM measurement, the films were grown on the 20 nm thick Si₃N₄ electron transparent membranes. The pressure of the Ar gas was 0.4 Pa. The base pressure was lower than 2×10^{-5} Pa. The LTEM measurements were performed in a FEI Titan Cs Probe TEM in Lorentz mode (the Fresnel imaging mode) at 300 kV. The images were obtained at a tilted angle and a defocus of 600 μm . The MFM measurements were carried out in a Dimension ICON probe microscopy system (ICON, Bruker, USA) and a scanning probe microscopy (MFP-3D, Asylum Research) at room temperature. The magnetic fields were applied by a self-built Helmholtz coil. The magnetic response was studied using standard magnetic Co/Al-coated cantilevers (SSS-MFMR, Nanosensors, 2.8 N m⁻¹ spring constant) in-phase mode and with a lift height of 30 nm. The transport measurements of MTJ were performed in the PPMS or the MFM that is upgraded with electrical measurement equipment.

Micromagnetic Simulations: The micromagnetic computations were carried out by means of a state-of-the-art micromagnetic solver, PETASPIN, which numerically integrates the Landau–Lifshitz–Gilbert (LLG) equation by applying the time solver scheme Adams–Bashforth.^[4,5]

$$\frac{d\mathbf{m}}{d\tau} = -(\mathbf{m} \times \mathbf{h}_{\text{eff}}) + \alpha_G \left(\mathbf{m} \times \frac{d\mathbf{m}}{d\tau} \right) \quad (1)$$

where α_G is the Gilbert damping, $\mathbf{m} = \mathbf{M}/M_s$ is the normalized magnetization, and $\tau = \gamma_0 M_s t$ is the dimensionless time, with γ_0 being the gyromagnetic ratio and M_s the saturation magnetization. \mathbf{h}_{eff} is the normalized effective magnetic field, which includes the exchange, interfacial DMI, magnetostatic, anisotropy, and external fields.^[2,6]

The skyrmion layer CoFeB/Ta/[Pt/Co/Ta]₁₀, by 1 layer of CoFeB with thickness 1.25 nm, 10 repetitions of a 2.5 nm thick Co ferromagnet separated by a 5 nm thick Ta/Pt non-magnetic layer, was simulated. Each ferromagnetic layer was coupled to the other ones by means of the magnetostatic field only (exchange decoupled). We used the same parameters for the CoFeB (similar to the previous study on Ta/CoFeB/MgO^[52]) and Co ferromagnets due to different thicknesses, namely saturation magnetization $M_s = 1200 \text{ kA m}^{-1}$, uniaxial perpendicular anisotropy constant $K_u = 0.91 \text{ MJ m}^{-3}$ (for Co, this had been selected after a systematic study to fit the experimental skyrmion diameter), exchange constant $A = 10 \text{ pJ m}^{-1}$, and interfacial DMI constant $D = 0.4 \text{ mJ m}^{-2}$ (for Co, this was in agreement with refs. [60,61]). A discretization cell size of 3 nm \times 3 nm \times 1.25 nm was used, and a system with a diameter of 1.2 μm , was simulated.

Analytical Skyrmion Profile: The polar angle $\Theta_0(r)$, that describes the skyrmion profile, is obtained from the following equilibrium equation

$$\nabla^2 \Theta_0 = \left(\xi^2 + \frac{1}{r^2} \right) \sin \Theta_0 \cos \Theta_0 - \frac{d}{r} \sin^2 \Theta_0 + h \sin \Theta_0 \quad (2)$$

that is calculated from the minimization of the energy functional.^[62] In Equation (2), $\xi^2 = Q - 1 = 2K_u/\mu_0 M_s^2 - 1$, $h = H_{\text{ext}}/M_s$, $r = \rho/l_{\text{ex}}$ is the reduced polar coordinate, and $d = |D|_{\text{ex}}/A$, where $l_{\text{ex}} = \sqrt{2A/\mu_0 M_s^2}$ is the exchange length. An approximated solution of Equation (2) can be found by using the following ansatz:^[62]

$$\tan \frac{\Theta_0(r)}{2} = \frac{r_{\text{sk}}}{r} e^{\xi(r_{\text{sk}} - r)} \quad (3)$$

where $r_{\text{sk}} = R_{\text{sk}}/l_{\text{ex}}$ is the reduced equilibrium skyrmion radius, defined as $m_z(r_{\text{sk}}) = 0$, in correspondence of the energetic minimum. For these parameters, $\xi = 0.156$ and $R_{\text{sk}} = 70.07 \text{ nm}$.

Supporting Information

Supporting Information is available from the Wiley Online Library or from the author.

Acknowledgements

This work was supported by the Beijing Natural Science Foundation (Grant No. Z190009), the Science Center of the National Science Foundation of China (Grant No. 52088101), the National Natural Science Foundation of China (Grants Nos. 11874409, 52161160334, and 12174426), the K. C. Wong Education Foundation (Grant No. GJTD-2019-14), and the financial support of the Shenzhen Peacock Group Plan (Grant No. KQTD20180413181702403). G.F. and R.T. acknowledge the project “ThunderSKY,” funded by the Hellenic Foundation for Research and Innovation (HFRI) and the General Secretariat for Research and Technology (GSRT), under grant agreement No. 871. G.F., M.C., and R.T. also acknowledge the research project No. PRIN 2020LWPKH7 funded by the Italian Ministry of University and Research. X.Z. acknowledge the financial support by King Abdullah University of Science and Technology (KAUST), Office of Sponsored Research (OSR) under Award No. CRF-2019-4081-CRG8.

Conflict of Interest

The authors declare no conflict of interest.

Author Contributions

G.Y. conceived the idea and design the experiments. The study was performed under the supervision of G.Y. G.Y. designed the MTJ film structures. Y.Z. prepared the MTJ films with supports from Y.G., G.Y., S.Z., and X.Z. Y.G. and G.Y. performed the magnetic characterization of MTJ films. L.Z. fabricated the MTJ devices with supports from Z.Z. J.Z. performed the TEM measurements with supports from G.Y., Y.G., Y.P., and X.Z. Y.G. and Y.W. performed the MFM imaging measurements and the simultaneous transport measurements with support from G.Y., Z.H., and J.L. Y.G. performed the additional transport measurements with the support from G.Y., B.H., J.L., Y.L., J.F., H.W., J.M.D.C., and X.H. R.T., M.C., and G.F. performed the micromagnetic simulations. G.Y. and G.F. drafted the paper and all authors commented on the manuscript.

Data Availability Statement

The data that support the findings of this study are available from the corresponding author upon reasonable request.

Keywords

electron beam lithography, magnetic skyrmions, magnetic tunnel junction, skyrmion lattice, transmission electron microscopy

Received: May 23, 2022

Revised: July 30, 2022

Published online: September 23, 2022

- [1] N. Nagaosa, Y. Tokura, *Nat. Nanotechnol.* **2013**, *8*, 899.
- [2] A. Fert, N. Reyren, V. Cros, *Nat. Rev. Mater.* **2017**, *2*, 17031.
- [3] A. Fert, V. Cros, J. Sampaio, *Nat. Nanotechnol.* **2013**, *8*, 152.
- [4] J. Sampaio, V. Cros, S. Rohart, A. Thiaville, A. Fert, *Nat. Nanotechnol.* **2013**, *8*, 839.
- [5] G. Yu, P. Upadhyaya, Q. Shao, H. Wu, G. Yin, X. Li, C. He, W. Jiang, X. Han, P. K. Amiri, K. L. Wang, *Nano Lett.* **2017**, *17*, 261.
- [6] D. Bhattacharya, S. A. Razavi, H. Wu, B. Dai, K. L. Wang, J. Atulasimha, *Nat. Electron.* **2020**, *3*, 539.
- [7] J. Grollier, D. Querlioz, K. Y. Camsari, K. Everschor-Sitte, S. Fukami, M. D. Stiles, *Nat. Electron.* **2020**, *3*, 360.
- [8] J. Zazvorka, F. Jakobs, D. Heinze, N. Keil, S. Kromin, S. Jaiswal, K. Litzius, G. Jakob, P. Virnau, D. Pinna, K. Everschor-Sitte, L. Rozsa, A. Donges, U. Nowak, M. Klau, *Nat. Nanotechnol.* **2019**, *14*, 658.
- [9] G. Finocchio, M. Di Ventura, K. Y. Camsari, K. Everschor-Sitte, P. K. Amiri, Z. M. Zeng, *J. Magn. Magn. Mater.* **2021**, *521*, 167506.
- [10] S. Mühlbauer, B. Binz, F. Jonietz, C. Pfleiderer, A. Rosch, A. Neubauer, R. Georgii, P. Boni, *Science* **2009**, *323*, 915.
- [11] X. Z. Yu, Y. Onose, N. Kanazawa, J. H. Park, J. H. Han, Y. Matsui, N. Nagaosa, Y. Tokura, *Nature* **2010**, *465*, 901.
- [12] X. Z. Yu, N. Kanazawa, Y. Onose, K. Kimoto, W. Z. Zhang, S. Ishiwata, Y. Matsui, Y. Tokura, *Nat. Mater.* **2011**, *10*, 106.
- [13] K. Shibata, X. Z. Yu, T. Hara, D. Morikawa, N. Kanazawa, K. Kimoto, S. Ishiwata, Y. Matsui, Y. Tokura, *Nat. Nanotechnol.* **2013**, *8*, 723.
- [14] S. Seki, X. Z. Yu, S. Ishiwata, Y. Tokura, *Science* **2012**, *336*, 198.
- [15] A. K. Nayak, V. Kumar, T. Ma, P. Werner, E. Pippel, R. Sahoo, F. Damay, U. K. Rößler, C. Felser, S. S. P. Parkin, *Nature* **2017**, *548*, 561.
- [16] J. Jena, R. Stinshoff, R. Saha, A. K. Srivastava, T. P. Ma, H. Deniz, P. Werner, C. Felser, S. S. P. Parkin, *Nano Lett.* **2020**, *20*, 59.
- [17] L. Peng, R. Takagi, W. Koshibae, K. Shibata, K. Nakajima, T. H. Arima, N. Nagaosa, S. Seki, X. Yu, Y. Tokura, *Nat. Nanotechnol.* **2020**, *15*, 181.
- [18] N. Romming, C. Hanneken, M. Menzel, J. E. Bickel, B. Wolter, K. von Bergmann, A. Kubetzka, R. Wiesendanger, *Science* **2013**, *341*, 636.
- [19] S. Heinze, K. von Bergmann, M. Menzel, J. Brede, A. Kubetzka, R. Wiesendanger, G. Bihlmayer, S. Blugel, *Nat. Phys.* **2011**, *7*, 713.
- [20] W. Jiang, P. Upadhyaya, W. Zhang, G. Yu, M. Jungfleisch, F. Fradin, Y. Pearson, Y. Tserkovnyak, K. Wang, O. Heinonen, S. te Velthuis, A. Hoffmann, *Science* **2015**, *349*, 283.
- [21] C. Moreau-Luchaire, C. Moutafis, N. Reyren, J. Sampaio, C. Vaz, N. Van Horne, K. Bouzehouane, K. Garcia, C. Deranlot, P. Warnicke, P. Wohlhuter, J. George, M. Weigand, J. Raabe, V. Cros, A. Fert, *Nat. Nanotechnol.* **2016**, *11*, 731.
- [22] S. Woo, K. Litzius, B. Kruger, M. Im, L. Caretta, K. Richter, M. Mann, A. Krone, R. Reeve, M. Weigand, P. Agrawal, I. Lemesch, M. Mawass, P. Fischer, M. Klau, G. Beach, *Nat. Mater.* **2016**, *15*, 501.
- [23] O. Boulle, J. Vogel, H. Yang, S. Pizzini, D. Chaves, A. Locatelli, T. Montes, A. Sala, L. Buda-Prejbeanu, O. Klein, M. Belmeguenai, Y. Roussigne, A. Stashkevich, S. Cherif, L. Aballe, M. Foerster, M. Chshiev, S. Auffret, I. Miron, G. Gaudin, *Nat. Nanotechnol.* **2016**, *11*, 449.
- [24] G. Yu, P. Upadhyaya, X. Li, W. Li, S. K. Kim, Y. Fan, K. L. Wong, Y. Tserkovnyak, P. K. Amiri, K. L. Wang, *Nano Lett.* **2016**, *16*, 1981.
- [25] A. Soumyanarayanan, M. Raju, A. L. G. Oyarce, A. K. C. Tan, M. Y. Im, A. P. Petrovic, P. Ho, K. H. Khoo, M. Tran, C. K. Gan, F. Ernult, C. Panagopoulos, *Nat. Mater.* **2017**, *16*, 898.
- [26] G. Q. Yu, A. Jenkins, X. Ma, S. A. Razavi, C. L. He, G. Yin, Q. M. Shao, Q. L. He, H. Wu, W. J. Li, W. J. Jiang, X. F. Han, X. Q. Li, A. C. B. Jayich, P. K. Amiri, K. L. Wang, *Nano Lett.* **2018**, *18*, 980.
- [27] Y. Guang, I. Bykova, Y. Liu, G. Yu, E. Goering, M. Weigand, J. Gräfe, S. K. Kim, J. Zhang, H. Zhang, Z. Yan, C. Wan, J. Feng, X. Wang, C. Guo, H. Wei, Y. Peng, Y. Tserkovnyak, X. Han, G. Schütz, *Nat. Commun.* **2020**, *11*, 949.
- [28] J. Liu, Z. Wang, T. Xu, H. Zhou, L. Zhao, S.-G. Je, M.-Y. Im, L. Fang, W. Jiang, *Chin. Phys. Lett.* **2022**, *39*, 017501.
- [29] A. Neubauer, C. Pfleiderer, B. Binz, A. Rosch, R. Ritz, P. G. Niklowitz, P. Boni, *Phys. Rev. Lett.* **2009**, *102*, 186602.
- [30] D. Liang, J. P. DeGrave, M. J. Stolt, Y. Tokura, S. Jin, *Nat. Commun.* **2015**, *6*, 8217.
- [31] C. Hanneken, F. Otte, A. Kubetzka, B. Dupe, N. Romming, K. von Bergmann, R. Wiesendanger, S. Heinze, *Nat. Nanotechnol.* **2015**, *10*, 1039.
- [32] H. F. Du, D. Liang, C. M. Jin, L. Y. Kong, M. J. Stolt, W. Ning, J. Y. Yang, Y. Xing, J. Wang, R. C. Che, J. D. Zang, S. Jin, Y. H. Zhang, M. L. Tian, *Nat. Commun.* **2015**, *6*, 7637.
- [33] D. Macchiello, W. Legrand, N. Reyren, K. Garcia, K. Bouzehouane, S. Collin, V. Cros, A. Fert, *Nat. Nanotechnol.* **2018**, *13*, 233.
- [34] K. Zeissler, S. Finizio, K. Shahbazi, J. Massey, F. Al Ma'Mari, D. M. Bracher, A. Kleibert, M. C. Rosamond, E. H. Linfield, T. A. Moore, J. Raabe, G. Burnell, C. H. Marrows, *Nat. Nanotechnol.* **2018**, *13*, 1161.
- [35] A. F. Scarioni, C. Barton, H. Corte-Leon, S. Sievers, X. K. Hu, F. Ajejas, W. Legrand, N. Reyren, V. Cros, O. Kazakova, H. W. Schumacher, *Phys. Rev. Lett.* **2021**, *126*, 077202.
- [36] Z. D. Wang, M. H. Guo, H. A. Zhou, L. Zhao, T. Xu, R. Tomasello, H. Bai, Y. Q. Dong, S. G. Je, W. L. Chao, H. S. Han, S. Lee, K. S. Lee, Y. Y. Yao, W. Han, C. Song, H. Q. Wu, M. Carpentieri, G. Finocchio, M. Y. Im, S. Z. Lin, W. J. Jiang, *Nat. Electron.* **2020**, *3*, 672.
- [37] W. Koshibae, Y. Kaneko, J. Iwasaki, M. Kawasaki, Y. Tokura, N. Nagaosa, *Jpn. J. Appl. Phys.* **2015**, *54*, 053001.
- [38] R. Tomasello, M. Ricci, P. Burrascano, V. Puliafito, M. Carpentieri, G. Finocchio, *AIP Adv.* **2017**, *7*, 056022.
- [39] G. Finocchio, F. Buttner, R. Tomasello, M. Carpentieri, M. Klau, *J. Phys. D: Appl. Phys.* **2016**, *49*, 423001.
- [40] N. E. Penthorn, X. Hao, Z. Wang, Y. Huai, H. W. Jiang, *Phys. Rev. Lett.* **2019**, *122*, 257201.
- [41] S. Kasai, S. Sugimoto, Y. Nakatani, R. Ishikawa, Y. K. Takahashi, *Appl. Phys. Express* **2019**, *12*, 083001.
- [42] S. Li, A. Du, Y. Wang, X. Wang, X. Zhang, H. Cheng, W. Cai, S. Lu, K. Cao, B. Pan, N. Lei, W. Kang, J. Liu, A. Fert, Z. Hou, W. Zhao, *Sci. Bull.* **2022**, *67*, 691.
- [43] X. C. Zhang, M. Ezawa, Y. Zhou, *Sci. Rep.* **2015**, *5*, 9400.
- [44] P. Upadhyaya, G. Q. Yu, P. K. Amiri, K. L. Wang, *Phys. Rev. B* **2015**, *92*, 134411.
- [45] M. Carpentieri, R. Tomasello, R. Zivieri, G. Finocchio, *Sci. Rep.* **2015**, *5*, 16184.
- [46] Y. Zhou, E. Iacocca, A. A. Awad, R. K. Dumas, F. C. Zhang, H. B. Braun, J. Åkerman, *Nat. Commun.* **2015**, *6*, 8193.
- [47] G. Finocchio, M. Ricci, R. Tomasello, A. Giordano, M. Lanuzza, V. Puliafito, P. Burrascano, B. Azzerboni, M. Carpentieri, *Appl. Phys. Lett.* **2015**, *107*, 262401.
- [48] Y. Q. Huang, W. Kang, X. C. Zhang, Y. Zhou, W. S. Zhao, *Nanotechnology* **2017**, *28*, 08LT02.

- [49] K. M. Song, J. S. Jeong, B. Pan, X. C. Zhang, J. Xia, S. Cha, T. E. Park, K. Kim, S. Finizio, J. Raabe, J. Chang, Y. Zhou, W. S. Zhao, W. Kang, H. S. Ju, S. Woo, *Nat. Electron.* **2020**, 3, 148.
- [50] X. C. Zhang, Y. Zhou, K. M. Song, T. E. Park, J. Xia, M. Ezawa, X. X. Liu, W. S. Zhao, G. P. Zhao, S. Woo, *J. Phys.: Condens. Matter* **2020**, 32, 143001.
- [51] W. Legrand, J. Y. Chauleau, D. Maccariello, N. Reyren, S. Collin, K. Bouzehouane, N. Jaouen, V. Cros, A. Fert, *Sci. Adv.* **2018**, 4, eaat0415.
- [52] W. Li, I. Bykova, S. Zhang, G. Yu, R. Tomasello, M. Carpentieri, Y. Liu, Y. Guang, J. Grafe, M. Weigand, D. M. Burn, G. van der Laan, T. Hesjedal, Z. Yan, J. Feng, C. Wan, J. Wei, X. Wang, X. Zhang, H. Xu, C. Guo, H. Wei, G. Finocchio, X. Han, G. Schutz, *Adv. Mater.* **2019**, 31, 1807683.
- [53] A. O. Mandru, O. Yildirim, R. Tomasello, P. Heistracher, M. Penedo, A. Giordano, D. Suess, G. Finocchio, H. J. Hug, *Nat. Commun.* **2020**, 11, 6365.
- [54] S. F. Zhang, J. W. Zhang, Y. Wen, E. M. Chudnovsky, X. X. Zhang, *Appl. Phys. Lett.* **2018**, 113, 192403.
- [55] S. F. Zhang, J. W. Zhang, Q. Zhang, C. Barton, V. Neu, Y. L. Zhao, Z. P. Hou, Y. Wen, C. Gong, O. Kazakova, W. H. Wang, Y. Peng, D. A. Garanin, E. M. Chudnovsky, X. X. Zhang, *Appl. Phys. Lett.* **2018**, 112, 132405.
- [56] J. Z. S. Zhang, Y. Wen, E. M. Chudnovsky, X. Zhang, *Commun. Phys.* **2018**, 1, 36.
- [57] S. D. Pollard, J. A. Garlow, J. W. Yu, Z. Wang, Y. M. Zhu, H. Yang, *Nat. Commun.* **2017**, 8, 14761.
- [58] Y. Guang, K. Ran, J. Zhang, Y. Liu, S. Zhang, X. Qiu, Y. Peng, X. Zhang, M. Weigand, J. Grafe, G. Schutz, G. van der Laan, T. Hesjedal, S. Zhang, G. Yu, X. Han, *Phys. Rev. Lett.* **2021**, 127, 217201.
- [59] Y. M. Huai, H. D. Gan, Z. H. Wang, P. F. Xu, X. J. Hao, B. K. Yen, R. Malmhall, N. Pakala, C. Wang, J. Zhang, Y. C. Zhou, D. H. Jung, K. Satoh, R. J. Wang, L. Xue, M. Pakala, *Appl. Phys. Lett.* **2018**, 112, 092402.
- [60] L. Wang, C. Liu, N. Mehmood, G. Han, Y. D. Wang, X. L. Xu, C. Feng, Z. P. Hou, Y. Peng, X. S. Gao, G. H. Yu, *ACS Appl. Mater. Interfaces* **2019**, 11, 12098.
- [61] G. Carlotti, A. Magni, A. Casiraghi, E. Darwin, G. Durin, L. H. Diez, B. J. Hickey, A. Huxtable, C. Y. Hwang, G. Jakob, C. Kim, M. Kläui, J. Langer, C. H. Marrows, H. T. Nembach, D. Ravelosona, G. A. Riley, J. M. Shaw, V. Sokalski, S. Tacchi, M. Kuepferling, arXiv:2201.04925, **2022**.
- [62] R. Tomasello, K. Y. Guslienko, M. Ricci, A. Giordano, J. Barker, M. Carpentieri, O. Chubykalo-Fesenko, G. Finocchio, *Phys. Rev. B* **2018**, 97, 060402(R).